Experimental characterization of the combustion dynamics of a subscale rocket combustor operating with gaseous methane and gaseous, subcritical or transcritical oxygen

Stéphane Boulal, Nicolas Fdida, Lucien Vingert, Miguel Martin-Benito

EXPERIMENTAL CHARACTERIZATION OF THE COMBUSTION DYNAMICS OF A SUBSCALE ROCKET COMBUSTOR OPERATING WITH GASEOUS METHANE AND GASEOUS, SUBCRITICAL OR TRANSCRITICAL OXYGEN

SPACE PROPULSION 2022
ESTORIL, PORTUGAL | 09 - 13 MAY 2022

Stéphane Boulal[(1)], **Nicolas Fdida**[(1)], **Lucien Vingert**[(1)], and **Miguel Martin-Benito**[(2)]

[(1)]*DMPE, ONERA, Université Paris Saclay, F-91123 Palaiseau, France,*
email: stephane.boulal@onera.fr
[(2)]*CNES, Launchers Directorate, Paris, France*

KEYWORDS: Liquid Rocket Engine, Methane oxy-combustion, Liquid oxygen, Atomization, Low-Frequency Instability

ABSTRACT:

The present experimental study, carried out on the Mascotte test bench of ONERA, aims at characterizing the flame and flow dynamics of a rocket-type combustor equipped with five shear-coaxial injectors fed with methane and oxygen. Backlit and OH* chemiluminescence imaging techniques are used for the characterization of the liquid atomization and flame dynamics obtained with three canonical cases labeled after the thermodynamic state at which oxygen is injected: gaseous, subcritical or transcritical, whereas methane is continuously injected at a gaseous state. For gaseous-oxygen operating conditions, a Low-Frequency flapping instability of the flame was observed and analyzed by means of the Spectral Proper Orthogonal Decomposition (SPOD) technique. For subcritical pressure, the atomization process is characterized by measuring the liquid core length and by providing a probabilistic description of the spray.

1. INTRODUCTION

In the frame of the European Space Agency (ESA) Future Launchers Preparatory Program (FLPP), a new generation of engines propelled by liquid oxygen (LOx) and methane (CH_4) for reusable launchers is under study within the Prometheus demonstrator development. The use of LOx/CH_4 in future combustion devices brings new specific challenges. The common CNES/ONERA C3PO (*Combustion Cryotechnique CH4 plus Oxygène*) research program aims at addressing part of these challenges.

Liquid Rocket Engine operate in a large domain of conditions [1]. Besides, if the engine is of the gas-generator type, the propellants are burning in different mixture ratio ranges, e.g., fuel-rich in the gas-generator and near-stoichiometric fuel-rich in the main combustion chamber. Also, depending on the engine operation, the thermodynamic state of the propellants can either be gaseous, liquid (subcritical or transcritical) or supercritical. For over 15 years, The Mascotte facility has been continuously employed to study methane oxy-combustion phenomena. These are, for example, (i) the flame structure under various combinations of CH_4/O_2 injection regimes [1–4], (ii) the liquid propellant(s) atomization [5], (iii) the High-Frequency (HF) instabilities [6, 7] or (iv) the heat transfer at the combustion chamber walls [8]. In addition, these studies have been used as validation cases of numerous numerical works [1,9–17]. There is still a need for the qualification of LRE-combustor's transitory phases, whereby the thermodynamic state of the propellants may affect the flame behavior. The present experimental work is motivated by (i) the visualization of the flame and flow dynamics at canonical operating conditions based on the thermodynamic state of the oxygen, namely the gaseous, subcritical and transcritical states and (ii) the analysis of the transition from the gaseous to the subcritical states and from the subcritical to the transcritical states.

The present article is structured as follows. In Section 2, we describe the Mascotte facility, the subscale combustion chamber employed, the optical diagnostics set to image the combustion and liquid jet dynamics, namely OH* chemiluminescence and backlit visualizations, and the operating conditions achieved during the campaign. In Section 3, we present the experimental results. More specifically, we compare cases and their associated transient operations to one another. The transitions from gaseous to liquid and from subcritical to transcritical states are also qualitatively described. In Section 4, we analyze a Low-Frequency (LF) instability observed in gaseous conditions by means of the Spectral Proper Orthogonal Decomposition (SPOD) technique. Finally, the atomization process is characterized by (i) measuring the liquid-core length and (ii) providing a probabilistic description of the spray.

2. EXPERIMENTAL SETUP

2.1. The Mascotte facility and the Bhp-HrM combustion chamber

Developed at ONERA in the early '90s, the Mascotte facility is a unique test rig (in France) designed to investigate the fundamental aspects of cryogenic combustion [18, 19]. As opposed to actual LREs, the bench is highly instrumented with a myriad of sensors (pressure transducers, flowmeters, thermocouples, fluxmeters). It is fitted with optical accesses allowing for non-intrusive investigations

of cryogenic combustion.

The combustion chamber used in this study is specifically designed to run at high pressure and high mixture ratios. It is called *Boitier Haute Pression et Haut Rapport de Mélange* or Bhp-HrM for short and is displayed in Fig. 1. Share-funded by CNES and ONERA, it has been used in previous test campaigns [8, 20–22]. It consists of a 615-mm long horizontal tube composed of interchangeable modules of 56-mm circular cross-section. The pro-

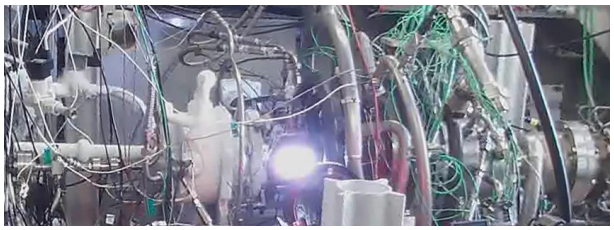

Figure 1: The Bhp-HrM combustion chamber.

pellants, i.e., the oxygen and the methane, are fed to the chamber through five shear-coaxial injectors mounted with no recess in an "X" arrangement, i.e., with a central injector located at the center of a circle whereby the four others are symmetrically positioned. A shear-coaxial injector consists of two concentric tubes whose inner and outer parts are respectively fed with oxygen and methane. The inner tube diameter is noted d and will be used in the following for all non-dimensionalizations. The inner and outer diameters of the methane annulus are, respectively, $1.2d$ and $1.5d$.

Each propellant is fed from a pressurized vessel where it is stored in gaseous or liquid form. For the oxygen, the injection circuit is jacket-cooled by means of liquid nitrogen (N_2) so as to ensure the fluid remains in liquid form. In this work, methane of purity > 99% is consistently injected in the gaseous state at ambient temperature, and oxygen is either injected in the gaseous state at ambient temperature or in the liquid state at a temperature of $\sim$ 100 K (see §2.3).

A visualization module is placed just downstream of the injection plate ($x = 0$ plane). It is equipped with two lateral 40-mm-thick quartz visualization windows mounted on opposed optical ports. Their inner faces are film-cooled by injecting a helium (He) layer through the slit formed at the interface between the injection and visualization modules. In general, the helium film-cooling mass flow is set to between five and ten percent of the total mass flow. From the combustion-chemistry viewpoint, helium does not affect the behavior of the flames since it is chemically inert. The remaining ports, i.e., the bottom and top ones are, respectively, equipped with a plain flange fitted with thermocouples, and a flange whereby an ignition torch is mounted to establish the combustion in the chamber. The torch comprises a small pilot chamber, which is fed with gaseous hydrogen and gaseous oxygen. The mixture is spark-ignited, and the resulting jet flame directs towards the main CH_4/O_2 jets at a 90° angle. A thermal measurement module is located downstream of the visualization module. It is equipped with various thermocouples to characterize the wall heat transfers. We will not present those measurements here, but a thorough characterization in a similar configuration and at various operating conditions can otherwise be found in [8]. At the back-end, a converging nozzle completes the assembly. Each module is water-cooled in order to sustain the harsh environment within the combustion chamber.

2.2. Dual high-speed visualizations

Simultaneous backlit and OH* chemiluminescence imaging techniques are employed to visualize the flame and atomization dynamics. Their principles are schematically represented in Fig. 2.

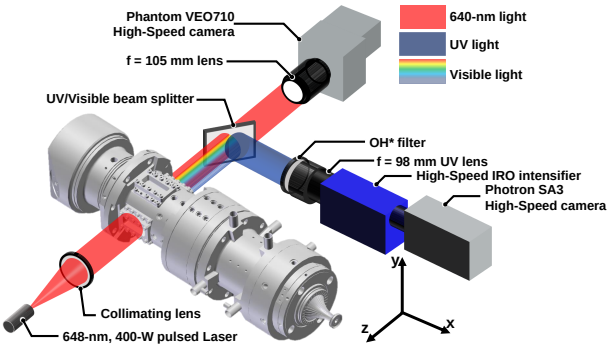

Figure 2: Schematic view of the dual high-speed visualization setup.

Backlit imaging consists of visualizing the shades formed by the dense liquid phase upon irradiance from a collimated beam. The backlit effect is created employing a Cavilux Smart 400-W laser, which emits pulsed incoherent monochromatic light of 648$\pm$10 nm-wavelength. On the opposite side of the visualization module, a beam splitter separates the light - comprising that coming from the laser source and that emitted by the combustion - into a transmitted component in the visible range and a reflected component in the Ultraviolet (UV) range. The latter is used for the OH* chemiluminescence imaging (see below). The transmitted visible component is focused towards a Phantom VEO710 High-Speed camera through a $f = 105$-mm-lens (f/5.6). The camera is equipped with a CMOS sensor providing a 1280$\times$800 pixels-image-definition. The camera/lens combination provides a field of view covering the whole visualization window, with a resolution of 96 µm/pixel. The camera is set to the 1-µs-minimum exposure time to limit the amount of flame emission collected. The laser pulse duration – set to 40 ns – controls the exposure. It acts as a shutter by kinetically freezing the flow's liquid region, ensuring satisfactory time resolution.

OH* chemiluminescence imaging consists of visualizing the excited hydroxyl radical (OH*) produced by the combustion chemical reactions. Spontaneous emission of OH* occurs in the near UV between 300 and 325 nm [23–27]. OH* chemiluminescence imaging is line-of-sight integrated. Hence, it does not constitute a spatially-resolved quantity, as opposed to OH-PLIF. In practice, the OH* emission is spectrally selected – from the reflected UV beam – by means of a narrow-band filter of 310 nm-central wavelength, 10-nm-FWHM and 70-percent-maximum transmission. A Photron Fastcam SA3 High-Speed camera coupled to a Lavision HS-IRO image-intensifier then collects the OH* signal. The gate-opening time of the intensifier is set to 700 ns. The camera is equipped with a 12-bits-ADC sensor, which provides a 1024$\times$512 pixels-image-definition, with an exposure time of 2 µs. A $f = 98$-mm-UV lens (f/8) is mounted on the intensified camera allowing a 80 µm/pixel-image-resolution.

Both cameras operate at an acquisition rate of 1 kHz,

allowing a recording duration of approximately 10 s. They are time-synchronized, and their fields of view are carefully adjusted to match one another. On the backlit imaging, the 1-kHz-acquisition rate is too low to allow for the tracking of individual liquid elements (droplets or ligaments). To overcome this limitation, we performed reruns (see §2.3) and operated the backlit camera at an acquisition rate of 15 kHz.

We also employed a conventional video camera (not represented in Fig. 2) to image the combustion chamber at a 25-Hz-frame-rate and a 100-µs-exposure-time. It monitors the rig operation in real-time and provides a complementary three-dimensional insight into the combustor.

2.3. Operating conditions

During the test campaign reported in this work, we focused on three operating conditions. They are labeled after the thermodynamic state attained by the oxygen injection. These are the Gaseous Case, the Subcritical Case and the Transcritical Case. We have retained the transcritical labeling convention introduced in [28], considering that the supercritical state is, by strict thermodynamic definition, only achieved when both the fluid pressure and temperature are above critical values ($P_c^{O2} = 5.042$ MPa, $T_c^{O2} = 154.5$ K). In our study, the oxygen injection temperature remained below its critical value, which justifies the labeling convention. Tab. 1 summarizes the experimental conditions of the three cases reported in the study. The indicated values represent the time-averaged quantities reached during the stabilized plateau, characterized by quasi-steady values only varying to within one percent of the mean. On average, this lasted for $\sim$ 5 s, except for the Gaseous Case, which lasted $\sim$ 8 s. Fig. 3 gives the trajectory of the Transcritical Case run in the Pressure-Temperature diagram. The oxygen density is computed for illustrative purposes, assuming a Peng-Robinson Equation of State [29]. On top of the thermodynamic conditions, Tab. 1 additionally provides the values of the non-dimensional numbers classically used to characterize the injection conditions and atomization regime of shear-coaxial injectors [30–32]. These are:

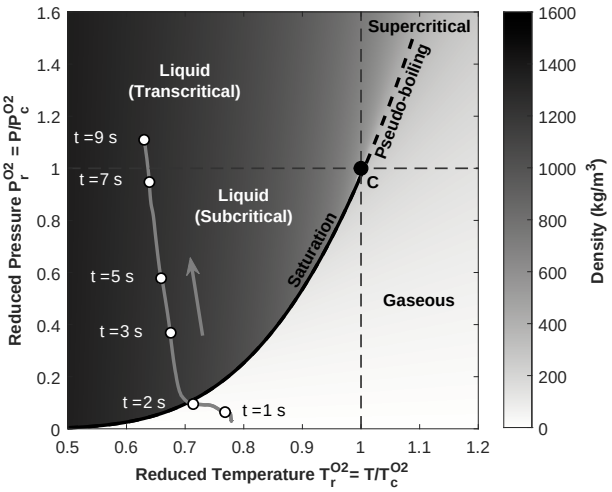

*Figure 3: Trajectory (gray line) of the **Transcritical Case** in the Pressure-Temperature diagram of oxygen. The oxygen density is determined assuming a Peng-Robinson Equation of State.*

(i) the Mixture Ratio MR $= \dot{m}_{O2}/\dot{m}_{CH4}$, with $\dot{m}_{O2}$ and $\dot{m}_{CH4}$ the O_2 and CH_4 mass flows. For reference, the values of the global Equivalence Ratio $\phi = MR_{st}/MR$, where MR_{st} =4 is the stoichiometric mixture ratio, are also provided.

(ii) the Velocity Ratio VR $= U_{CH4}/U_{O2}$, with U_{O2} and U_{CH4} the O_2 and CH_4 injection velocities.

(iii) the Momentum Flux Ratio $J = \rho_{CH4} U_{CH4}^2/\rho_{O2} U_{O2}^2$, with ρ_{O2} and ρ_{CH4} the O_2 and CH_4 densities.

(iv) the aerodynamic Weber number We $= \rho_{CH4} U_{CH4}^2 d/\sigma_{O2}$, with σ_{O2} the O_2 surface tension.

(v) the O_2 flow-based Reynolds number Re $= \rho_{O2} U_{O2} d/\mu_{O2}$, with μ_{O2} the O_2 dynamic viscosity.

For each case, we conducted at least two repetitions of the same experiments. For the Transcritical Case rerun, we operated the recording of the backlit camera at the 15-kHz-acquisition rate. The methane is continuously injected at room temperature in the gaseous state, except for the Transcritical Case, which achieved a strict supercritical state with both pressure and temperature stabilizing above the methane critical values ($P_c^{CH4} = 4.599$ MPa, $T_c^{CH4} = 190.6$ K). For all the cases considered, the stabilized-plateau value of the Mixture Ratio is at a relatively constant value of MR $\approx$ 2.3. According to the classification of shear-coaxial atomization regimes proposed in [30], fiber-type atomization is expected and is indeed observed. It manifests by the production of thin and short liquid fibers peeling off from the liquid-core periphery as soon as the liquid jet exits the nozzle [33].

Fig. 4 compares visualizations of the combustor (in true colors), as imaged by the conventional video camera, for conditions of gaseous, subcritical and transcritical oxygen-injection.

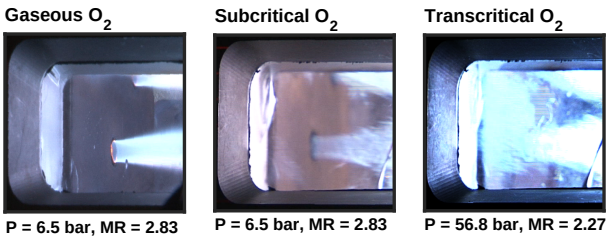

*Figure 4: True-colors visualizations of the combustor for conditions of **gaseous** (left), **subcritical** (middle) and **transcritical** (right) oxygen injection.*

3. RESULTS

3.1. General descriptions and comparisons

For the three cases, Fig. 5 shows the evolution of the pressure P within the combustion chamber. For the Subcritical and Transcritical cases, the evolution of the oxygen saturation pressure P_{sat}^{O2} is also plotted. Ramping-ups of the pressure are achieved in two stages. The torch operates between $t = -0.4$ s and $t = 2$ s. The recording triggers at $t = 0$ s. Stabilized plateau is achieved at $t \approx 7$ s for the Gaseous Case and $t \approx 10$ s for the Subcritical and Transcritical cases. This difference is due to the longer time required to stabilize the liquid-oxygen mass flow. Two

Table 1: Experimental conditions (plateau-averaged values) of the cases reported, ***P****: combustion chamber pressure,* $T_{inj.}^{O2}$*:* O_2 *injection temperature,* **MR***: Mixture Ratio,* ϕ*: Global Equivalence Ratio,* **VR***: Velocity Ratio,* ***J****: Momentum Flux Ratio,* **We***: Aerodynamic Weber number,* **Re***:* O_2*-injection-based Reynolds number.*

Case	P (MPa)	$T_{inj.}^{O2}$ (K)	MR	ϕ	VR	J	We	Re
● **Gaseous**	4.42	290	2.29	1.75	0.96	0.5	n/a	3.7×10^5
● **Subcritical**	4.38	93	2.25	1.78	19.7	9.9	1.1×10^4	4.0×10^4
● **Transcritical**	5.77	95	2.27	1.76	15.1	7.5	1.7×10^4	5.9×10^4

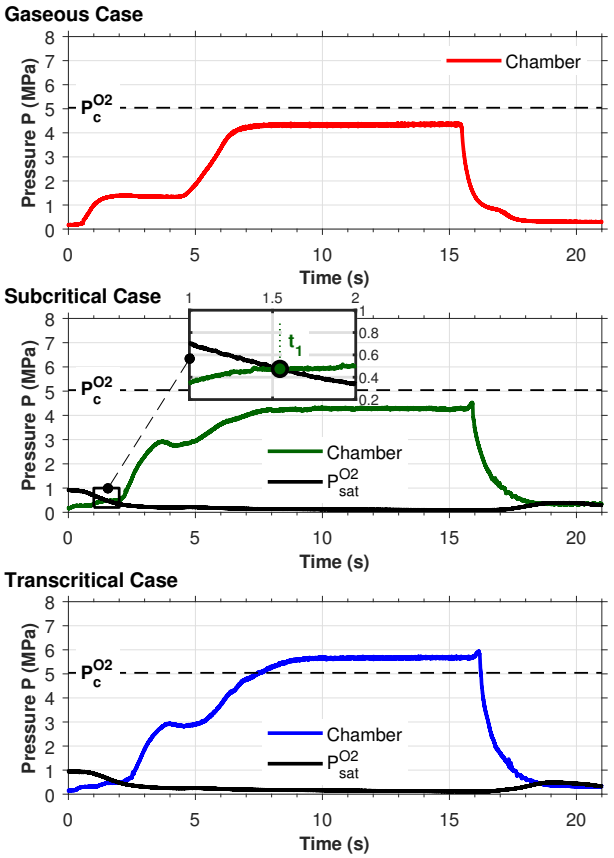

Figure 5: Evolution of the pressure in the combustion chamber for the ***Gaseous*** *(top),* ***Subcritical*** *(middle) and* ***Transcritical*** *(bottom) cases.* P_c^{O2}*: oxygen critical pressure.* P_{sat}^{O2}*: oxygen saturation pressure.*

characteristic times t_1 and t_2 are shown in Fig. 5. The first one is the time at which the chamber pressure exceeds the oxygen-saturation pressure, i.e., when the condensation of the oxygen begins. The second one is the time at which the chamber pressure reaches the oxygen critical pressure. We will use these times to locate and portray the two transitions described in §3.2.

Fig. 6 shows instantaneous images from both high-speed recordings of the three studied cases, taken within their respective stabilized plateaux. The ($x = 0$) plane and the ($y = 0$) axis are, respectively, the injection plane and the central-injector axis. The OH* chemiluminescence intensity is represented in false colors and, for each case, the intensity is normalized by its maximum to provide higher contrast. All the cases resulted in the flame anchoring at the injector lip, as observed on the OH* chemiluminescence visualizations. This can also be observed on the true-colors visualizations of Fig. 4. Flame closure always occurs downstream of the visualization zone, and we could therefore not ascertain its position.

Predictably enough, the backlit imaging recorded for the Gaseous Case does not return any useful information except for some water droplets condensing at the windows. The OH* chemiluminescence image shows an off-axis central flame and part of the bottom surrounding one(s). The deviation of the flame from the injector axis is actually due to a Low-Frequency instability locked inside the combustion chamber, which we further analyze in §4.1.

The Subcritical Case resulted in a crack of the foreground visualization window. It is partially tarnishing both visualizations for $6 < x/d < 12$. The backlit visualization shows a dark-horizontal central region corresponding to the liquid-oxygen jet core. It is surrounded by the gaseous methane jet, which is observable at upstream positions ($0 < x/d < 3$) because of its high density. The OH* chemiluminescence image shows an intense heat release zone located in the second half of the visualized zone. This is due to the delay imposed by the processes of atomization, vaporization and mixing. The flame radial extent is larger in the Subcritical Case than in the Gaseous Case. This is due to oxygen droplets pulling out from the central region.

For the Transcritical Case, we switched the background and foreground windows to obtain better-quality images. This is why the crack no longer appears on the OH* chemiluminescence visualization. On the backlit visualization, the interface of the liquid-oxygen core is not as sharp as that observed for the Subcritical Case. The intense region of OH* emission has progressed upstream as a result of the disappearance of the surface tension when the pressure goes supercritical (see §3.2). In addition, the flame cone appears to be wider. This observation is confirmed on the OH* chemiluminescence image since the flames of the bottom injectors are discernible, indicating an expansion of each flame in the radial direction. The dynamics of the transition from subcritical to transcritical regimes are further discussed in §3.2.

3.2. Transitional Dynamics

Oxygen condensation and flame anchoring

For the Subcritical Case, Fig. 7 gives composite images of OH* chemiluminescence and backlit visualizations, which we constructed by snipping both visualizations along the central injector axis. According to Fig. 5, the oxygen condensation (saturation) occurs around $t = t_1 = 1.554$ s, which is in agreement with the appearance of the liquid jet in Fig. 7, between $t = 1.536$ s and $t = 1.770$ s. On both frames, we note the presence of the GH_2/GO_2 flame flowing from the torch at $x/d \approx 10$.

The oxygen condensation occurs before the flame stabilizes at the injector lip, which is observed on the following frames. The stabilization of the flame results from the rapid deflagration of the premixed reactants present in the

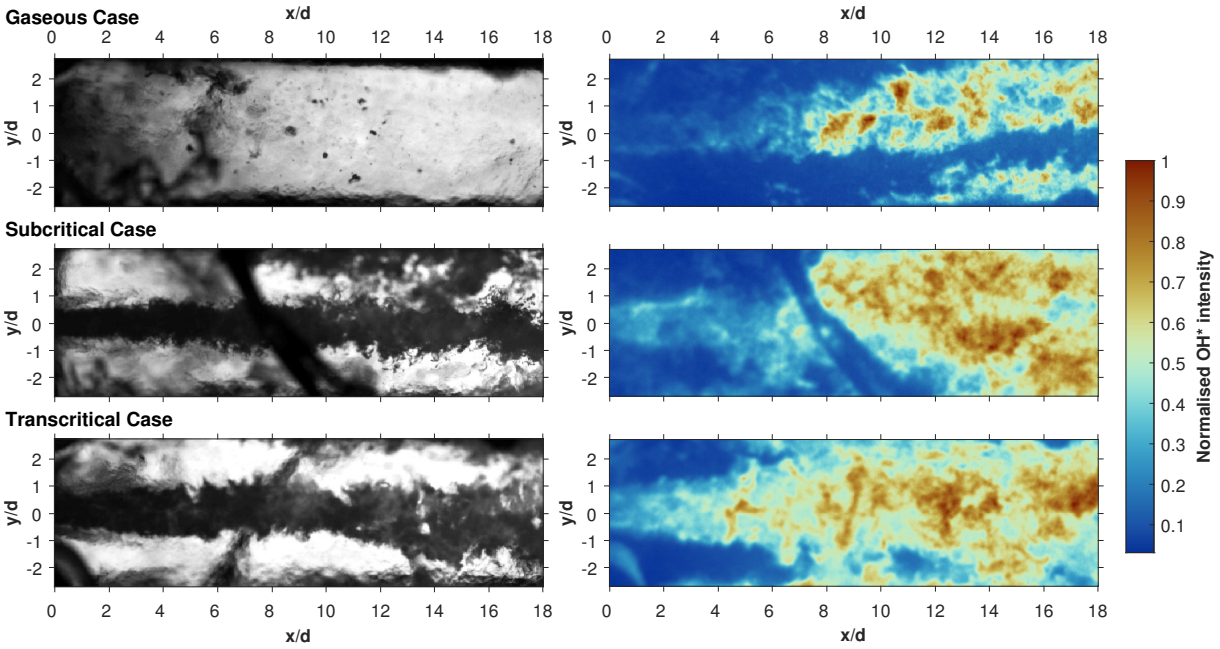

*Figure 6: Comparisons of **backlit** (left column) and **OH* chemiluminescence** (right column) instantaneous images (within stabilized plateaux) for the **Gaseous** (top row), **Subcritical** (middle row) and **Transcritical** (bottom row) cases.*

outer recirculation zone. In agreement with the mechanism described in [34, 35], the flame front originated from a region ignited by the torch (possibly that surrounding the bottom jets), progressed upstream, reached the injector inner lip and anchored in the vicinity of the oxygen-core boundary. During this highly transient process, we observe, e.g., at time $t_1 = 2.059$ s, the complete disappearance of the liquid-oxygen core. We understand this to be consecutive to the deflagration propagation, which imposes a pressure close to the injector face plate larger than the oxygen injection pressure, causing the oxygen flow to disrupt temporarily. This pressure peak is, however, not observed on the pressure recording (see Fig. 5), presumably because the only pressure tapping within the combustion chamber is located further downstream, at $x/d = 75$. After a period of $\sim$ 10ms, the liquid-oxygen jet develops again but is now coexistent with the anchored flame.

Critical pressure crossing

For the Transcritical Case, Fig. 8 provides a series of backlit visualizations showing the dynamic evolution of the jet as the oxygen approaches and crosses the transcritical state. The values of the oxygen and methane reduced pressure, $P_r^{O2} = P/P_c^{O2}$ and $P_r^{CH4} = P/P_c^{CH4}$, are also displayed. For low values of P_r^{O2}, the liquid-oxygen jet features the classical morphology of fiber-type atomization, with ligaments and droplets peeling out from the dense-oxygen core. Along the jet axis, the interface appears to be increasingly corrugated, resulting from the instability developing at the interface. The droplets produced by the primary atomization further reduce in size through vaporization to the surrounding hot gas or through the secondary breakup mechanism, which fragments them into lower-diameter droplets. As the chamber pressure approaches the oxygen-critical pressure, i.e., $P_r^{O2} \rightarrow 1$, we observe the progressive evolution of the liquid-oxygen interface from a sharp and highly corrugated one to a diffuse and smooth one. When the critical pressure is exceeded, a considerably lower number of oxygen lumps (fibers and droplets) detach from the core region. Instead, the liquid-oxygen core appears to get crumbled from the outside. This is explained by the reduction of the liquid surface tension and latent heat of vaporization to near-zero values as P_r^{O2} approaches unity. In such conditions where the surface tension has vanished, the vaporization process is considerably accelerated. We illustrate this point in Fig. 9, where we compare the evolutions of single-detached oxygen droplets at subcritical and supercritical pressure. The latter is characterized by non-spherical droplets detaching from the core, which rapidly diffuse, mix and burn with the methane. In fact, the process of vaporization, which characterizes subcritical-type injection, does not exist anymore at supercritical pressure. Instead, it is replaced by the so-called pseudo-boiling, which, phenomenologically, reduces to gas-like diffusion and mixing.

Simultaneously, as the pressure increases, the methane jet appears to get darker (see Fig. 8) as a consequence of an increase in its density. At respectively transcritical and supercritical conditions, the mixing between O_2 and CH_4 resembles more to that found in the shear layer between two turbulent gaseous streams of large density and velocity differences. As a matter of fact, the shapes obtained at the interface recall that of the Kelvin-Helmholtz (KH) hydrodynamic instability.

4. ANALYSIS

4.1. Gaseous Case Low-Frequency instability

For the Gaseous Case operation, we observed the establishment of a Low-Frequency (LF) instability of the central flame and possibly of the surrounding ones. The instability triggers as soon as the flame anchors at the injector lip and continuously subsists during the pressure ramps and the plateau period. It manifests as a transverse flapping motion of the flame as shown in Fig. 10, which

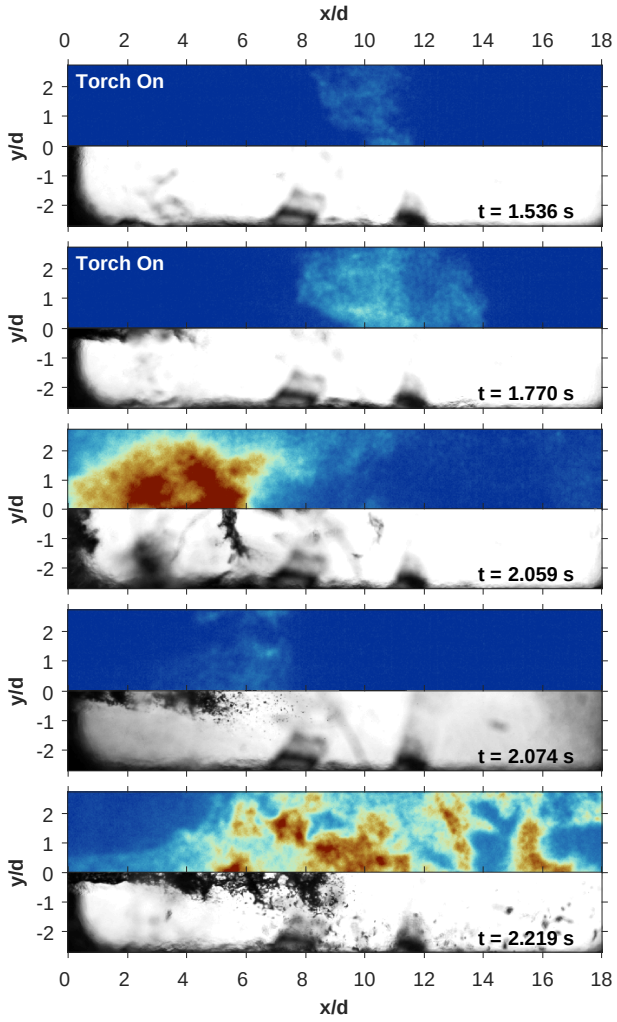

*Figure 7: Series of **OH* chemiluminescence** (top) and **backlit** (bottom) composite images of the **Subcritical** Case dynamically showing the oxygen-jet condensation and the flame anchoring at the central injector lip.*

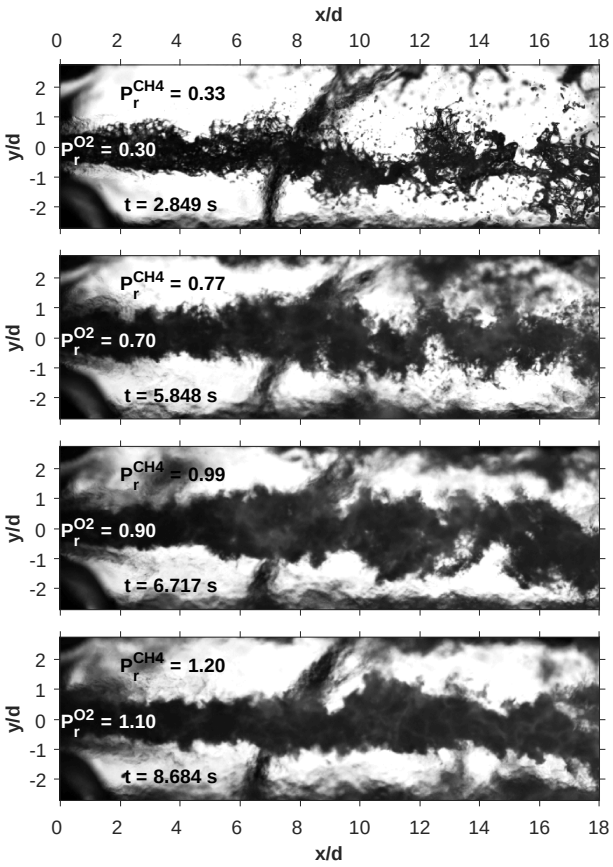

*Figure 8: Series of backlit visualizations dynamically showing the evolution of the oxygen from **subcritical** to **transcritical** conditions.*

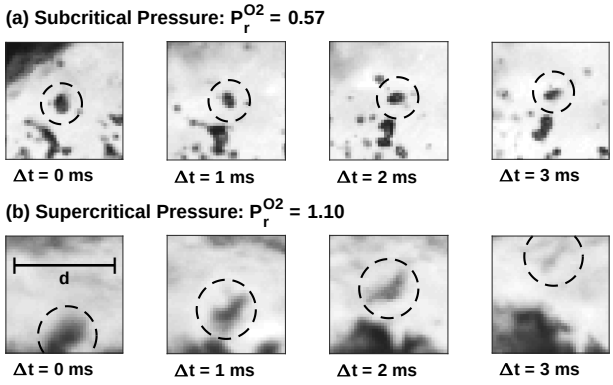

*Figure 9: Single-droplet evolution at **subcritical (a)** and **supercritical (b)** pressure. Tracking of the droplets is performed on the 15-kHz-recording of the Transcritical Case 2. The frame of reference is moving with the droplet. Δt: local time frame. d is the injector inner tube diameter.*

provides consecutive OH* chemiluminescence snapshots taken within the stabilized plateau. Because OH* chemiluminescence is a 2D representation of a 3D phenomenon, we could only observe a transverse motion of the flame. Since the geometry is symmetric, we believe this motion could be that of a precession of the flame around the injector axis. In order to better understand the origin of the instability, the Spectral Proper Orthogonal Decomposition (SPOD) technique, in the form developed in [36], is performed on the OH* chemiluminescence recording. The SPOD technique aims at extracting coherent structures embedded within a flow, which *apriori* appears chaotic, e.g., acoustic induced resonance, vortex-shedding-type instabilities. We do not describe here the algebraic details of the technique. Thorough descriptions of modal decomposition methods applied to various fluid dynamics problems and comparisons between techniques could otherwise be found in [36, 37]. The SPOD method computes modes representing structures that evolve coherently both in space and time. We have applied the SPOD method on a series of $N_t = 3600$ images taken within the stabilized plateau, i.e., spanning 3.6 s of the recording. Fig. 11 (a) shows the frequency distribution (spectral density) of the most dominant ($m = 1$) SPOD-modes. We observe a frequency peak at $f = 93.75$ Hz. For this frequency, Fig. 11 (b) gives the distribution of the energy (the eigenvalues) between modes, normalized by the sum of the eigenvalues. The most dominant mode hence retains 60% of the energetic content at the $f = 93.75$-Hz-frequency. Finally, Fig. 11 (c) shows the mode's shape (real part) relative to the retained frequency. It indicates a transverse oscillatory motion which we associate with the flapping or precession instability.

A first explanation for this instability originates from the acoustic resonance of the O_2 feed line. As a matter of fact, Fig. 12 shows the FFT of the dynamic pressure recorded

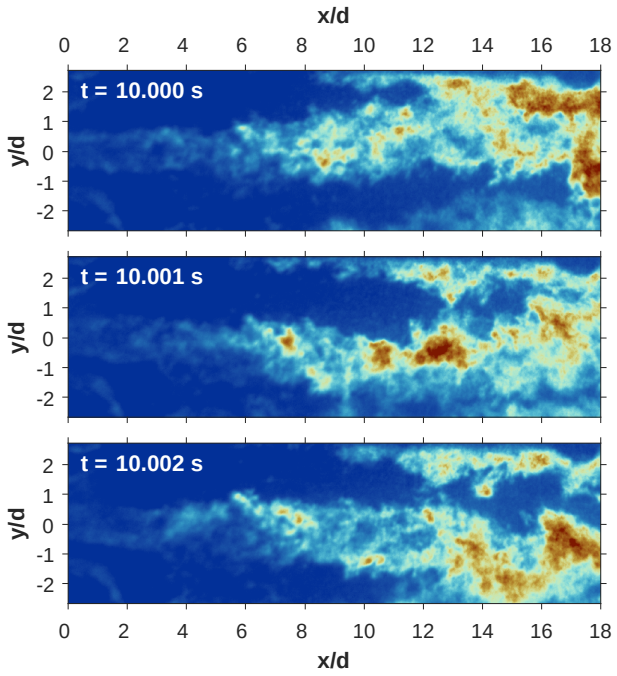

Figure 10: Series of OH chemiluminescence snapshots recorded during the stabilized plateau of the **Gaseous** Case. The time interval between snapshots is 1 ms.*

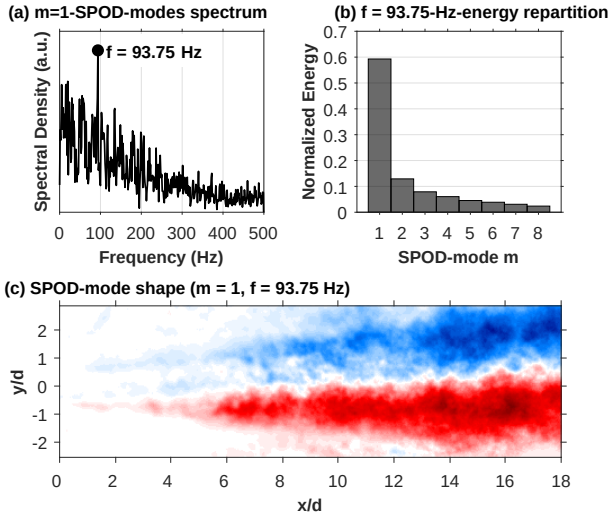

Figure 11: Spectral Proper Orthogonal Decomposition (SPOD) analysis performed on a sequence of OH chemiluminescence images within the **Gaseous** Case stabilized plateau. **(a)** Spectral Density of the most dominant ($m = 1$) SPOD-modes. **(b)** Normalized Energy distribution at the $\boldsymbol{f} = 93.75$-Hz-frequency. **(c)** Shape of the most dominant SPOD-mode at the $\boldsymbol{f} = 93.75$-Hz-frequency.*

in the O_2 feed line. The frequency peak found at 96 Hz well coincides with the oscillation frequencies found by the SPOD analysis. Note that the peak-to-peak amplitude of this oscillation is only about 0.7% of the mean pressure. On the other hand, considering that the feed line could be modeled as a closed-open cavity between the sonic throat located upstream and the injection plate, the eigenfrequencies of the longitudinal modes are determined according to:

$$f_{nL} = \frac{(2n-1)a_{sound}}{4L_{line}} \qquad \text{(Eq.1)}$$

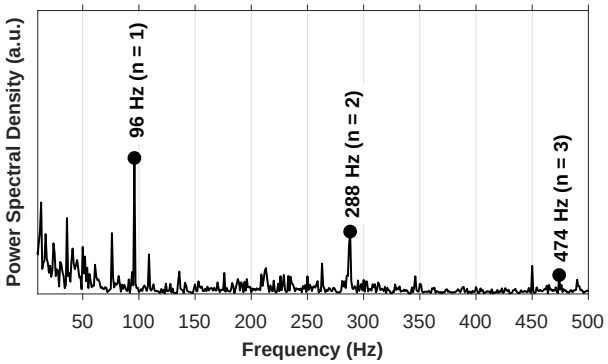

*Figure 12: Fast Fourier Transform (FFT) of the oxygen feed line dynamic pressure recorded during the **Gaseous** Case stabilized plateau.*

where a_{sound} is the speed of sound in the oxygen and L_{line} is the length of the oxygen feed line. This is measured from the position of the upstream sonic throat down to the injection plate. Tab. 2 provides the values of the first three eigenfrequencies ($n = 1, 2, 3$). These correspond to the

Table 2: Theoretical values of the first three ($\boldsymbol{n} = 1, 2, 3$) acoustic eigenfrequencies of the oxygen feed line.

	$n = 1$	$n = 2$	$n = 3$
f_{nL} (Hz)	94.6	283.7	472.8

clear-cut frequency peaks observed in Fig. 12. It is, however, still unclear how this longitudinal acoustic resonance resulted in a precession or flapping motion in the combustion chamber.

A second explanation is of hydrodynamic nature. Indeed, in [38], the authors have observed a similar instability in a multiple-injectors arrangement using a lean premixed methane-air mixture. The so-called confinement-induced instability is reported to occur at a characteristic Strouhal number $\mathrm{St} = 0.012$, albeit they also observed this phenomenon for $0.001 < \mathrm{St} < 0.01$ in previous studies. In our case, considering the oxygen nozzle diameter and injection velocity, we find that the instability occurs at a Strouhal number of $\mathrm{St} = fd/U_{O2} = 0.008$, which is in agreement with the observations of [38].

4.2. Primary-atomization description

In order to quantitatively describe the primary breakup atomization process, we propose to determine the liquid core length L. It is classically defined [32] as the maximum downstream position above which the liquid core starts to fragment into droplets and ligaments, i.e., above which the liquid jet no longer forms a continuous phase. In Fig. 13, we illustrate the procedure to extract this length. First, the backlit image is binarized using the Matlab global thresholding algorithm based on Otsu's method [39]. On top of the binarized image, we draw a fan of lines spreading across the spray cone. We then look for the line that maximally and continuously covers the binarized liquid region, and we measure the length L along. For the Subcritical Case, Fig. 14 gives the evolution of L (symbols). The instantaneous measurement constitutes quite a fluctuating signal with amplitudes of oscillation rising to $\sim 30\%$. We applied a moving average filter of 0.25-s-width to the measured data (the line in Fig. 14). For time $t > 5.5$s,

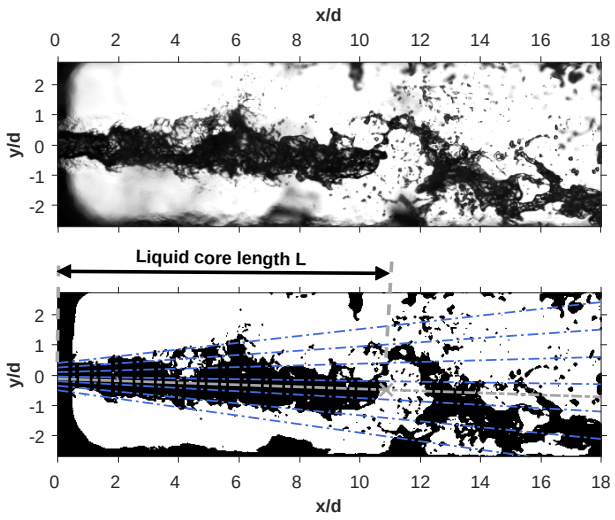

*Figure 13: Determination of the liquid core length **L**. **Top:** instantaneous backlit visualization. **Bottom:** corresponding binarized image.*

the complete breakup of the liquid jet intermittently occurs downstream of the visualization window and could therefore not be measured. In Fig. 14, we compare the measurements of L to a selection of semi-empirical correlations formulated in the literature for shear-coaxial injectors, namely those of Mayer [32], Eroglu et al. [40] and Davis and Chehroudi [41]. Tab. 3 provides details of each formulation. These correlations were proven to provide satisfactory agreement with experimental results obtained in the Mascotte bench [21]. Still, the comparison was, at that time, based on mean values, obtained on a steady atomizing LO_2/H_2 configuration, not the dynamically evolving configuration of the present work. In Fig. 14, the measured and correlations-derived values are of the same order magnitude, but their trends differ.

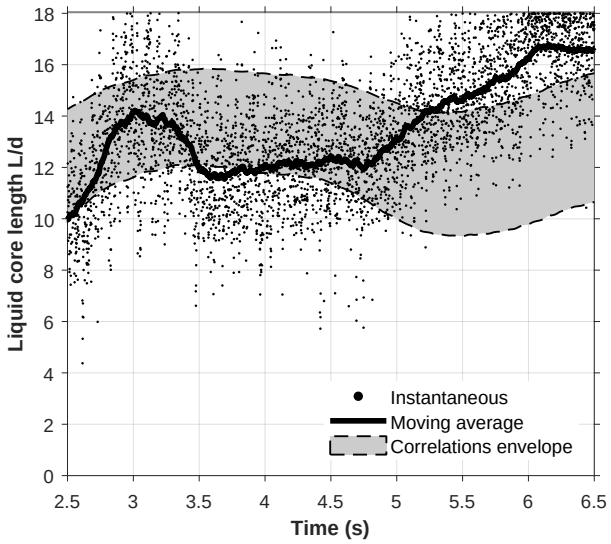

*Figure 14: Evolution of the liquid core length L (**Subcritical** Case) compared to that evaluated based on the semi-empirical correlations of Mayer [32], Eroglu et al. [40] and Davis and Chehroudi [41].*

In our case, we found that the liquid core length better and simply correlates to the inertia imposed to the liquid jet. That is, L is, on the first order, proportional to the injection velocity (based on the pressure-drop measurement across the injection plate, $\Delta P_{O2} = P_{O2} - P$):

$$\frac{L}{d} = k\sqrt{\frac{\Delta P_{O2}}{\rho_{O2}}} \qquad \text{(Eq.2)}$$

For each case where L could be experimentally determined, i.e., within the visualization region, we have approached the measurement of L with the correlation (Eq.2). Hence, Fig. 15 provides the measurement (moving-average filtered) of L and compares it to that estimated by the correlation (Eq.2). We consider the two reruns, numbered 1 and 2, of the Subcritical and Transcritical cases. We find that the correlation well reproduces the dynamic evolution of L. The correlation coefficient k is framed to a mean value $k = 0.61$ s/m and with satisfactory accuracy, as a standard deviation $\sigma_k = 0.0216$ s/m (3.5% of the mean) is obtained.

*Table 3: Semi-empirical correlations of Mayer [32], Eroglu et al. [40] and Davis and Chehroudi [41] for the determination of the liquid core length of shear-coaxial injectors. $\boldsymbol{C_1}$: adjustable constant, $\boldsymbol{J}$: Momentum Flux Ratio, σ: liquid surface tension, μ_L: liquid dynamic viscosity, **Re**: Liquid-injection-based Reynolds number, $\mathbf{We}_{\Delta U}$: Weber number based on the gaseous/liquid velocity difference.*

Reference	Correlation for L_b/d
Mayer [32]	$\frac{C_1}{J^{2/3}}\left(\frac{\sigma}{\mu_L U_L}\right)^{1/3}$
Eroglu et al. [40]	$0.66\mathrm{Re}^{0.6}\mathrm{We}_{\Delta U}^{-0.4}$
Davis and Chehroudi [41]	$25J^{-0.2}$

4.3. Probabilistic description of the spray

For the Transcritical Case 2 (Fig. 15 (d)), we observe a time period, between $t = 4.75$ s and $t = 5.5$ s (subcritical pressure), for which L is approximately constant. For this time period, we quantitatively characterize the atomization process through a probabilistic description of the spray. To that end, we use the objects detected using the binarization described above. For each detected object, we perform a circularity check in order to decide to count or discard it as a droplet. In addition, we used the gradient-based methodology proposed in [42] to discard out-of-focus objects. This inhibits the detection of the droplets originating from the outer-injectors jets. The backlit-imaging resolution is not sufficient to allow for the whole range of droplet diameter to be detected. The resulting droplet-diameter distributions are hence ill-characterized, i.e., truncated because of the detection limit and biased towards the larger diameters. As such, characteristic diameters, such as the Sauter Mean Diameter, could not be correctly determined. Some 11251 images, between $t = 4.75$ and $t = 5.5$ s, are used to populate the statistical sample. We choose to base the probabilistic description on the Transcritical Case 2 because it benefits from a higher sample size than the other 1-kHz-recordings. About 1.74 million droplets are thereby sampled, i.e., on average ~ 155 droplets are detected at each time step.

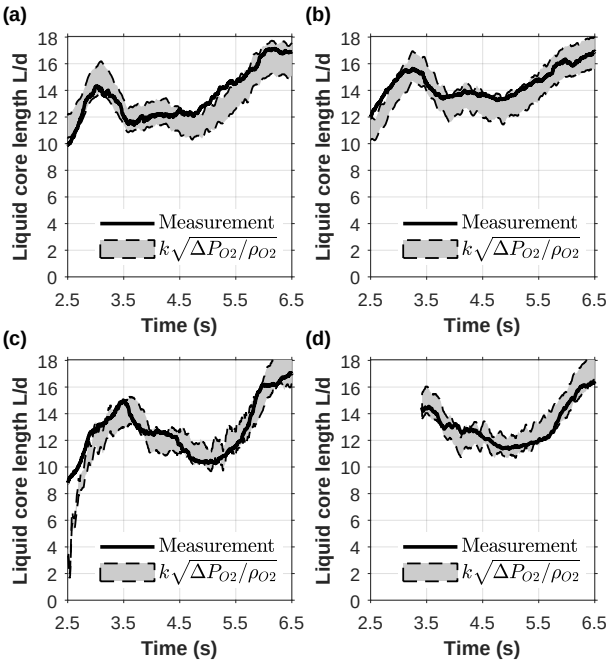

Figure 15: Comparisons between the dynamic measurements of the liquid core length ***L*** *and the proposed initial inertia-based correlation (Eq.2).* ***(a) Subcritical*** *Case 1.* ***(b) Subcritical*** *Case 2.* ***(c) Transcritical*** *Case 1.* ***(d) Transcritical*** *Case 2. The shaded areas correspond to the 95% Confidence Interval ($\pm 2\sigma_k$) of the correlation coefficient k.*

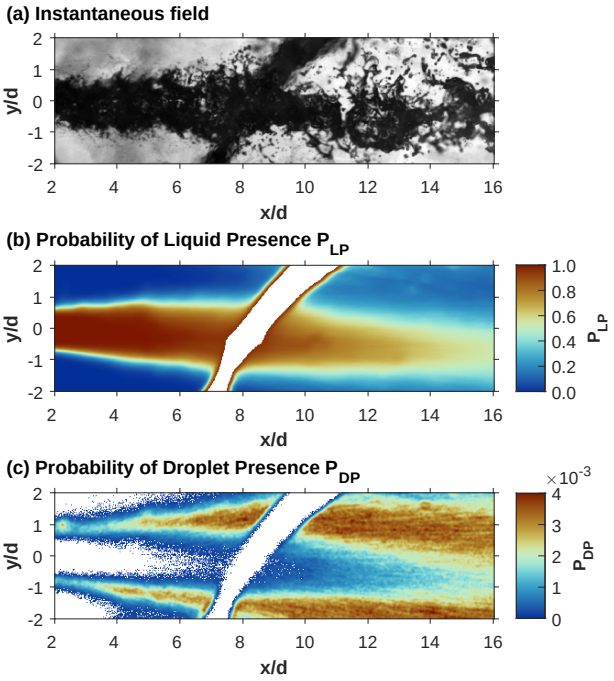

Figure 16: Probabilistic description of the spray for the subcritical time-period of the ***Transcritical*** *Case 2 recorded at 15 kHz. (a) Instantaneous backlit visualization. (b) Probability of Liquid Presence* $\boldsymbol{P_{LP}}$*. (c) Probability of Droplet Presence* $\boldsymbol{P_{DP}}$*. On subfigures (b) and (c), white areas correspond to regions where liquid or droplets are not detected, or their presence could not be correctly ascertained.*

Fig. 16 provides the fields of the probability of liquid presence P_{LP} and droplet presence P_{DP}. The Probability of Liquid Presence can alternatively be interpreted as the time-averaged liquid volume fraction. A Gaussian filter is applied to the P_{DP} fields to smooth out the noise. White regions are those where liquid or droplets are not detected, or their presence could not be correctly ascertained.

5. CONCLUSIONS

In this work, we have presented experimental results of an experimental investigation into the dynamics of a subscale rocket combustor operating with five shear-coaxial injectors fed with methane and oxygen. We have described three canonical cases, which we categorized according to the targeted pressure within the combustion chamber relative to the critical pressure of oxygen, namely the Gaseous Case, the Subcritical Case and the Transcritical Case. We simultaneously set OH* chemiluminescence and backlit recordings to visualize the central injector flame and the dynamics of the corresponding liquid jet.

One of the objectives of this communication is to document the transitional dynamics of the flame and liquid-oxygen jet when the combustor pressure exceeds the saturation and critical pressure of the oxygen. As for the former, the oxygen condensation always occurred before the flame had anchored at the injector lip. It would be interesting to observe the case where the flame stabilizes first (with gaseous oxygen injection), and the oxygen condensation follows. Regarding the second transition, backlit recordings provide valuable visualizations of the liquid-oxygen jet progression.

For the Gaseous Case, we observed a Low-Frequency instability on the OH* chemiluminescence recording. The instability manifests as a flapping or precession motion of the flame. We used the SPOD technique to analyze the instability. Note that we have also applied other modal decomposition techniques, i.e., standard POD and exact DMD. They essentially revealed the same dominant mode both spatially and spectrally. Hence, we isolated a structurally-coherent dominant mode of characteristic frequency $\sim$ 95 Hz. We found that this frequency coincides with the 1L acoustic mode eigenfrequency of the oxygen feed line. Alternatively, we observed that the instability well matched the so-called confinement hydrodynamic instability found in previous works [38]. Therefore, it could be the case that the hydrodynamic instability is responsible for amplifying the acoustic resonance in the oxygen feed line or that the acoustic resonance amplifies the hydrodynamic instability. Additionally, hydrodynamic coupling with the surrounding jets could also have a role in the instability. In order to decide which mechanism is at play, we could determine if the instability still manifests for different acoustic-resonant frequencies or Strouhal numbers. Finally, we still need to figure whether we observe the confinement-induced instability if a single-injector is used or in non-reactive conditions. Another open question is whether the flame had a flapping or precession motion. One way to answer this would be to image the combustion chamber either from the front or in two directions orthogonal to the chamber axis or to use the OH-PLIF imaging technique. Tiny asymmetrical elements, such as the cavity of the torch located on the top port of the combustor, could otherwise induce the break from symmetry.

Finally, we have provided quantitative analyses of the

atomization process. First, we dynamically measured the liquid core length. For this, we have proposed a new semi-empirical formulation for its dependency, which is proven better to match the measurement than those of previous works. Second, we provided a probabilistic description of the oxygen spray. The resolution of the backlit images was not sufficient enough to resolve all of the droplet sizes, which resulted in droplet-diameter distributions being truncated and biased. The distributions could be correctly measured by improving the image resolution, as in [5, 43] or through PDI measurements [5].

ACKNOWLEDGMENTS

This work was funded by ONERA, the French Aerospace Lab and CNES, the French National Space Agency, through the C3PO (*Combustion Cryotechnique CH4 plus Oxygène*) program. We gratefully acknowledge the technical supports of Éric Paux for the preparation of the test campaign. The preparation and conduct of the Mascotte test facility were made possible by the outstanding contribution of the late Franck Vannier. His technical ability and problem-solving skills will be truly missed. We wish to thank Dr. Zhiyao Yin for the fruitful discussion regarding the analysis of the Low-Frequency instability and its possible connection with the confinement-induced instability phenomenon. We would also like to thank Dr. Lionel Matuszewski and Dr. Robin W. Devillers for proofreading the article and for the valuable suggestions.

References

[1] M. Théron, M. Martin Benito, B. Vieille, L. Vingert, N. Fdida, Y. Mauriot, R. Blouquin, C. Seitan, M. Onori, and L. Lequette, "Experimental and numerical investigation of LOX/Methane Cryogenic Combustion at low mixture ratio," in *8th European Conference for Aeronautics and Space Sciences (EUCASS), Madrid, Spain*, p. ..., 2019.

[2] G. Singla, P. Scouflaire, C. Rolon, and S. Candel, "Transcritical oxygen/transcritical or supercritical methane combustion," *Proc. Combust. Inst.*, vol. 30, no. 2, pp. 2921–2928, 2005.

[3] S. Candel, M. Juniper, G. Singla, P. Scouflaire, and C. Rolon, "Structure and dynamics of cryogenic flames at supercritical pressure," *Combust. Sci. Technol.*, vol. 178, no. 1-3, pp. 161–192, 2006.

[4] G. Singla, P. Scouflaire, J. C. Rolon, S. Candel, and L. Vingert, "OH Planar Laser-Induced Fluorescence and Emission Imaging in High Pressure LOx/Methane Flames," *J. Propul. Power*, vol. 23, no. 3, pp. 593–602, 2007.

[5] N. Fdida, L. Vingert, Y. Mauriot, L. H. Dorey, and M. Théron, "Comparison of LOx/Methane and LOx/Hydrogen cryogenic spray combustion with simultaneous optical diagnostics," in *8th European Conference for Aeronautics and Space Sciences (EUCASS), Madrid, Spain*, 2019.

[6] F. Richecoeur, P. Scouflaire, S. Ducruix, and S. Candel, "High-Frequency Transverse Acoustic Coupling in a Multiple-Injector Cryogenic Combustor," *J. Propul. Power*, vol. 22, no. 4, pp. 790–799, 2006.

[7] Y. Méry, L. Hakim, P. Scouflaire, L. Vingert, S. Ducruix, and S. Candel, "Experimental investigation of cryogenic flame dynamics under transverse acoustic modulations," *C.R. Mec.*, vol. 341, no. 1, pp. 100–109, 2013.

[8] L. Vingert, P. Grenard, F. Lévy, A. Nicole, L. H. Dorey, and M. Martin Benito, "Heat Transfer Measurements in a Water-Cooled Rocket Combustion Chamber Operated with Oxygen/Methane Mixtures at the Mascotte Test Facility," in *32nd ISTS and 9th NSAT Joint Symposium, Fukui, Japan*, 2019.

[9] T. Schmitt, Y. Méry, M. Boileau, and S. Candel, "Large-Eddy Simulation of oxygen/methane flames under transcritical conditions," *Proc. Combust. Inst.*, vol. 33, no. 1, pp. 1383–1390, 2011.

[10] N. Guézennec, M. Masquelet, and S. Menon, "Large Eddy Simulation of Flame-Turbulence Interactions in a LOx-CH4 Shear Coaxial Injector," in *50th AIAA Aerospace Sciences Meeting, Nashville, TN, USA*, 2012.

[11] L. Hakim, T. Schmitt, S. Ducruix, and S. Candel, "Dynamics of a transcritical coaxial flame under a high-frequency transverse acoustic forcing: Influence of the modulation frequency on the flame response," *Combustion and Flame*, vol. 162, no. 10, pp. 3482–3502, 2015.

[12] C. Traxinger, J. Zips, and M. Pfitzner, "Thermodynamic analysis and large-eddy simulations of LOx-CH_4 and LOx-H_2 flames at high pressure," in *Joint Propulsion Conference, Cincinnati, OH, USA*, 2018.

[13] C. Traxinger, J. Zips, and P. M., "Single-Phase Instability in Non-Premixed Flames Under Liquid Rocket Engine Relevant Conditions," *J. Propul. Power*, vol. 35, no. 4, pp. 675–689, 2019.

[14] Müller, H. and Pfitzner, M., "Large-eddy simulation of transcritical liquid oxygen/methane jet flames," in *EUCASS Book Series - Advances in AeroSpace Sciences*, vol. 11, pp. 177–194, 2019.

[15] T. Schmitt, "Large-Eddy Simulations of the Mascotte Test Cases Operating at Supercritical Pressure," *Flow Turbul. Combust*, vol. 105, no. 1, pp. 159–189, 2020.

[16] C. Laurent, G. Staffelbach, F. Nicoud, and T. Poinsot, "Heat-release dynamics in a doubly-transcritical LO2/LCH4 cryogenic coaxial jet flame subjected to fuel inflow acoustic modulation," *Proc. Combust. Inst.*, vol. 38, no. 4, pp. 6375–6383, 2021.

[17] A. Nicole, L. H. Dorey, L. Vingert, and M. Théron, "LES Simulation For Evaluation Of Acoustic Response Of Subcritical Coaxial Flame Submitted To High-Frequency Acoustic Fields," in *Space Propulsion, Estoril, Portugal*, 2021.

[18] M. Habiballah, M. Orain, F. Grisch, L. Vingert, and P. Gicquel, "Experimental studies of high-pressure cryogenic flames on the mascotte facility," *Combust. Sci. Technol.*, vol. 178, no. 1-3, pp. 101–128, 2006.

[19] L. Vingert, G. Ordonneau, N. Fdida, and P. Grenard, "A Rocket Engine under a Magnifying Glass," *J. AerospaceLab*, vol. 11, 2016.

[20] G. Ordonneau, P. Hervat, L. Vingert, S. Petitot, and B. Pouffary, "First Results of Heat Transfer Measurements in a New Water-Cooled Combustor on the

Mascotte Facility," in *4th European Conference for Aeronautics and Space Sciences (EUCASS), St. Petersburg, Russia*, 2011.

[21] N. Fdida, L. Vingert, G. Ordonneau, and S. Petitot, "Coupling high-speed imaging diagnostics to study a LOX/GH2 flame in a high-pressure rocket combustor," in *5th European Conference for Aeronautics and Space Sciences (EUCASS), Munich, Germany*, 2013.

[22] P. Grenard, N. Fdida, L. Vingert, L. H. Dorey, L. Selle, and J. Pichillou, "Experimental Investigation of Heat Transfer in a Subscale Liquid Rocket Engine," *J. Propul. Power*, vol. 35, no. 3, pp. 544–551, 2019.

[23] G. Dieke and H. Crosswhite, "The ultraviolet bands of oh fundamental data," *J. Quant. Spectrosc. Radiat. Transfer*, vol. 2, no. 2, pp. 97–199, 1962.

[24] M. Juniper, A. Tripathi, P. Scouflaire, J.-C. Rolon, and S. Candel, "Structure of cryogenic flames at elevated pressures," *Proc. Combust. Inst.*, vol. 28, no. 1, pp. 1103–1109, 2000.

[25] W. Mayer, A. Schik, M. Schäffler, and H. Tamura, "Injection and Mixing Processes in High-Pressure Liquid Oxygen/Gaseous Hydrogen Rocket Combustors," *J. Propul. Power*, vol. 16, no. 5, pp. 823–828, 2000.

[26] J. Lux and O. Haidn, "Flame Stabilization in High-Pressure Liquid Oxygen/Methane Rocket Engine combustion," *J. Propul. Power*, vol. 25, no. 1, pp. 15–23, 2009.

[27] M. Lauer, M. Zellhuber, T. Sattelmayer, and C. J. Aul, "Determination of the Heat Release Distribution in Turbulent Flames by a Model Based Correction of OH* Chemiluminescence," in *Turbo Expo: Power for Land, Sea, and Air. Volume 2: Combustion, Fuels and Emissions, Parts A and B, Vancouver, Canada*, pp. 105–115, 2011.

[28] W. O. H. Mayer, A. H. A. Schik, B. Vielle, C. Chauveau, I. Gokalp, D. G. Talley, and R. D. Woodward, "Atomization and Breakup of Cryogenic Propellants Under High-Pressure Subcritical and Supercritical Conditions," *J. Propul. Power*, vol. 14, no. 5, pp. 835–842, 1998.

[29] D.-Y. Peng and D. B. Robinson, "A New Two-Constant Equation of State," *Ind. Eng. Chem. Res.*, vol. 15, no. 1, pp. 59–64, 1976.

[30] Z. Farago and N. Chigier, "Morphological classification of disintegration of round liquid jets in a coaxial air stream," *Atomization Sprays*, vol. 2, no. 2, pp. 137–153, 1992.

[31] E. J. Hopfinger, "Liquid Jet Instability and Atomization in a Coaxial Gas Stream," in *Advances in Turbulence VII, Saint-Jean-Cap-Ferrat, France*, pp. 69–78, 1998.

[32] J. C. Lasheras and E. J. Hopfinger, "Liquid Jet Instability and Atomization in a Coaxial Gas stream," *Annu. Rev. Fluid Mech.*, vol. 32, no. 1, pp. 275–308, 2000.

[33] N. Fdida, Y. Mauriot, L. Vingert, A. Ristori, and M. Théron, "Characterizing primary atomization of cryogenic LOX/Nitrogen and lox/helium sprays by visualizations coupled to phase doppler interferometry," *Acta Astronaut.*, vol. 164, pp. 458–465, 2019.

[34] V. Schmidt, J. Sender, and M. Oschwald, "Simultaneous observation of liquid phase distribution and flame front evolution during the ignition transient of a LOx/GH2-combustor," *J. Visualization*, vol. 4, pp. 365–372, 2001.

[35] O. Gurliat, V. Schmidt, O. Haidn, and M. Oschwald, "Ignition of cryogenic H2/Lox sprays," *Aerosp. Sci. Technol.*, vol. 7, no. 7, pp. 517–531, 2003.

[36] A. Towne, O. T. Schmidt, and T. Colonius, "Spectral proper orthogonal decomposition and its relationship to dynamic mode decomposition and resolvent analysis," *J. Fluid Mech.*, vol. 847, p. 821–867, 2018.

[37] K. Taira, S. L. Brunton, S. T. M. Dawson, C. W. Rowley, T. Colonius, B. J. McKeon, O. T. Schmidt, S. Gordeyev, V. Theofilis, and L. S. Ukeiley, "Modal Analysis of Fluid Flows: An Overview," *AIAA Journal*, vol. 55, no. 12, pp. 4013–4041, 2017.

[38] Z. Yin, P. Kutne, I. Boxx, and W. Meier, "Jet-oscillation-induced combustion dynamics in a multi-nozzle flox® combustor," in *Proceedings of the ASME Turbo Expo 2018: Turbomachinery Technical Conference and Exposition. Volume 4A: Combustion, Fuels, and Emissions. Oslo, Norway*, 2018.

[39] N. Otsu, "A Threshold Selection Method from Gray-Level Histograms," *IEEE Transactions on Systems, Man, and Cybernetics*, vol. 9, no. 1, pp. 62–66, 1979.

[40] H. Eroglu, N. Chigier, and Z. Farago, "Coaxial atomizer liquid intact lengths," *Phys. Fluids A*, vol. 3, no. 2, pp. 303–308, 1991.

[41] D. W. Davis and B. Chehroudi, "Measurements in an Acoustically Driven Coaxial Jet under Sub-, Near-, and Supercritical Conditions," *J. Propul. Power*, vol. 23, no. 2, pp. 364–374, 2007.

[42] P. Marmottant and E. Villermaux, "On spray formation," *J. Fluid Mech.*, vol. 498, p. 73–111, 2004.

[43] N. Fdida, L. Vingert, A. Ristori, and Y. L. Sant, "Droplet size and velocity measurements in a cryogenic jet flame of a rocket-type combustor using high-speed imaging," *Atomization Sprays*, vol. 26, no. 5, pp. 411–438, 2016.